NANO LETTERS

Letter

pubs.acs.org/NanoLett

Valley Pseudospin with a Widely Tunable Bandgap in Doped Honeycomb BN Monolayer

Zhigang Song,[†] Ziwei Li,[†,‡] Hong Wang,[§] Xuedong Bai,[∥,⊥] Wenlong Wang,[∥] Honglin Du,[†] Sunquan Liu,[†] Changsheng Wang,[†] Jingzhi Han,[†] Yingchang Yang,[†] Zheng Liu,[§] Jing Lu,*[,†,⊥] Zheyu Fang,*[,†,‡,⊥] and Jinbo Yang*[,†,⊥]

[†]State Key Laboratory for Mesoscopic Physics and School of Physics and [‡]Academy for Advanced Interdisciplinary Studies, Peking University, Beijing 100871, China

[§]Center for Programmable Materials, School of Materials Science and Engineering, Nanyang Technological University, Singapore 639798

[∥]Institute of Physics, Chinese Academy of Sciences, Beijing 100190, China

[⊥]Collaborative Innovation Center of Quantum Matter, Beijing 100871, China

Supporting Information

ABSTRACT: Valleytronics is a promising paradigm to explore the emergent degree of freedom for charge carriers on the energy band edges. Using ab initio calculations, we reveal that the honeycomb boron nitride (h-BN) monolayer shows a pair of inequivalent valleys in the vicinities of the vertices of hexagonal Brillouin zone even without the protection of the C_3 symmetry. The inequivalent valleys give rise to a 2-fold degree of freedom named the valley pseudospin. The valley pseudospin with a tunable bandgap from deep ultraviolet to far-infrared spectra can be obtained by doping h-BN monolayer with carbon atoms. For a low-concentration carbon periodically doped h-BN monolayer, the subbands with constant valley Hall conductance are predicted due to the interaction between the artificial superlattice and valleys. In addition, the valley pseudospin can be manipulated by visible light for high-concentration carbon doped h-BN monolayer. In agreement with our calculations, the circularly polarized photoluminescence spectra of the $B_{0.92}NC_{2.44}$ sample show a maximum valley-contrasting circular polarization of 40% and 70% at room temperature and 77 K, respectively. Our work demonstrates a class of valleytronic materials with a controllable bandgap.

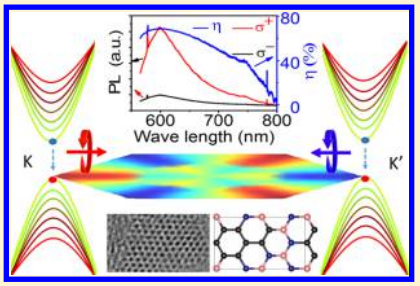

KEYWORDS: *Valleytronics, valley polarization, pseudospin, BNC monolayer, ab initio calculation, photoluminescence spectra*

The valley pseudospin, similar to real electron spin, is the degenerate energy extrema in momentum space and stands for a quantum degree of freedom. The manipulation and exploitation of valley pseudospin is the basis of valleytronics. Two-dimensional (2D) materials are a platform to realize valleytronic devices.[1−8] The known 2D valleytronic materials mainly include graphene/silicene and transition-metal dichalcogenide MX_2 (M = Mo, W, Cr; X = S, Se).[9,10] Valleys in these 2D materials are 2-fold degenerate but inequivalent extrema of the band structure at the hexagonal Brillouin zone corners (the K and K' points) due to the opposite Berry curvature. Berry curvature is a gauge-independent pseudovector that reflects the handedness and geometry of Bloch wave and can be viewed as a magnetic field in the reciprocal space.[11−13] The two-band $k\cdot p$ Hamiltonian describes the valley-contrasting physics very well based on the characteristic conditions, including the C_3 symmetry, inequivalent A−B sublattices, and direct bandgap.[11,14] The generation of valley polarization (nonequilibrium charge carrier distribution in two inequivalent valleys) by optical pumping technically requires a suitable bandgap. However, the bandgaps of graphene and silicene opened by a gentle perturbation that breaks inversion symmetry are very small (<0.3 eV).[15−17] The valley polarization and valley Hall effect are currently observed in 2D MX_2,[2] while the finite bandgap tuning via atomic doping and uncontrollable growth sector boundary restrict the applications of MX_2 monolayers in a narrow spectral range. Hence, it is very important to explore material systems beyond transition-metal dichalcogenides and graphene/silicene to meet the expectation of wide-spectral valleytronic applications with additional degrees of freedom.

Honeycomb boron nitride (h-BN) monolayers are usually used as substrates to investigate the valleytronic properties in graphene[18−20] and MX_2,[21] but the valley physics based on h-BN monolayer itself has long been neglected. The h-BN monolayer is a semiconductor with wide and direct bandgap of approximately 5.9 eV at the K and K' points, which demonstrates a great potential for the application as a deep-ultraviolet light emitter.[22] The large and direct bandgap is also beneficial to realize the valley pseudospin edge state and valleytronics in the ultraviolet region. In addition, the small

Received: January 19, 2017
Revised: February 7, 2017
Published: February 7, 2017

DOI: 10.1021/acs.nanolett.7b00271
Nano Lett. 2017, 17, 2079−2087

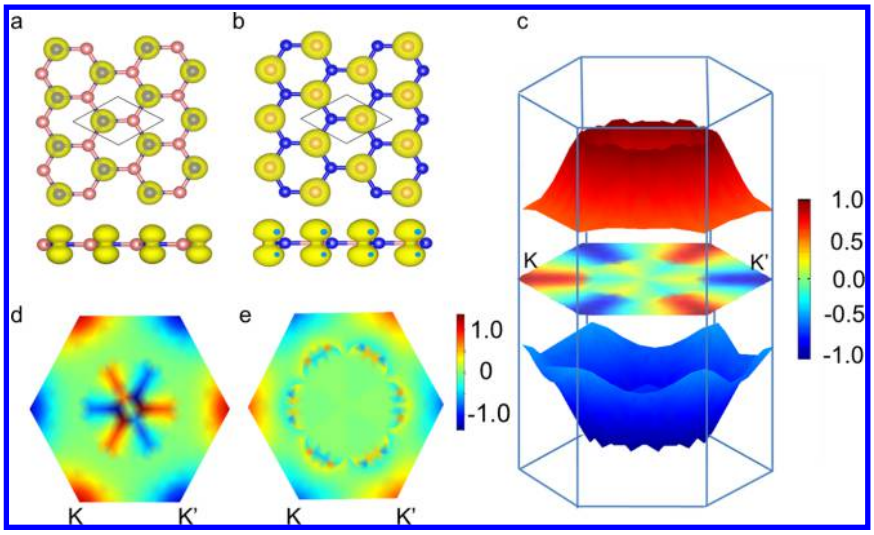

Figure 1. Valley-contrasting properties of intrinsic h-BN monolayer. (a, b) Top (up) and side (down) views of the crystal structure and electron density distribution of the VBM (a) and CBM (b). (c) Bottom conduction band (red) and top valence band (blue). The hexagon in the middle is the Brillouin zone color-coded by the degree of circular polarization. (d, e) Berry curvatures of the valence band (d) and the conduction band (e).

mismatch (~1.3%) with graphene makes h-BN monolayers an ideal platform for the fabrication of superlattices and metamaterials by hybridizing h-BN monolayer with graphene.[23−25] Various carbon-doped h-BN structures ($(BN)_x(C_2)_{1-x}$) have been synthesized by chemical vapor deposition (CVD).[23,24]

Here, we demonstrate that valleytronics with tunable bandgap from deep ultraviolet to far-infrared spectra can be realized in the $(BN)_x(C_2)_{1-x}$ monolayer by carefully controlling the atomic composition x using ab initio calculations. The valley polarization is robust against disorders and can survive even without the protection of C_3 symmetry. We also provide experimental evidence by measuring the circularly polarized photoluminescence (PL) in the prepared $B_{0.92}NC_{2.44}$ sample, which shows a valley polarization degree with a maximum value of 40% at room temperature and up to 70% at 77 K. In addition, our ab initio calculations indicate that their subbands contain discrete valley Hall conductance in periodically carbon-doped h-BN monolayer. Therefore, the valley Hall effect can exhibit a series of plateau with increasing carrier density owing to quasi-quantized Berry phase. Our investigation can be applied in a series of 2D materials, such as BP, BAs, BSb, GeC, SnC, SiC, $AgScP_2S_6$, $AgScP_2S_6$, and $CuSnP_2Se_6$ monolayers.

Valley-Contrasting Physical Properties in a Honeycomb Boron Nitride Monolayer. h-BN monolayer has a honeycomb crystal structure with each B atom occupying the center of a trigonal prismatic cage formed by three N atoms (Figure 1a,b). Similar to MX_2 monolayers, h-BN monolayer is a direct bandgap semiconductor and has two inequivalent valleys (Figure 1c) located in the vicinities of the vertices (K and K' points) of a hexagonal Brillouin zone (BZ). The minima of the conduction band (CBM), the maxima of the valence band (VBM), and their vicinities consist of the P_z orbit projected on the N atom for the VBM and the B atom for the CBM. Figure 1a,b shows the spatial distribution of valley electron density. The valley electrons in h-BN monolayer exhibit stronger spatial localization than those in graphene and MX_2 materials.

The time reversal symmetry and inversion asymmetry make the two valleys inequivalent, allowing valley-dependent manipulation. A hexagonal color map in the middle of Figure 1c shows the $\boldsymbol{k}$-resolved degree of circular polarization, which can be mathematically defined as

$$\eta(k) = \frac{|P_+(k)|^2 - |P_-(k)|^2}{|P_+(k)|^2 + |P_-(k)|^2} \quad (1)$$

where $P_\pm = P_x \pm P_y$ and P_α is the matrix element between the valence and conduction bands of the canonical momentum. The circular dichroism is perfectly valley-selective due to the protection by the C_3 symmetry. A left-handed (right-handed) circularly polarized photon can be selectively absorbed around the K' (K) point, while a right-handed (left-handed) one is completely prohibited. Therefore, the nonequilibrium charge carrier distribution in two inequivalent valleys can be generated (i.e., the generation of valley pseudospin polarization) by selective circularly polarized optical pumping. The perfect valley selection rule in h-BN monolayer provides potential applications in the valleytronic devices working in the deep ultraviolet region. Berry curvature is nonfigurative and has a mathematical expression of $\Omega(\mathbf{k}) = i\nabla_{\mathbf{k}} \times \langle u(\mathbf{k})|\nabla_{\mathbf{k}}|\mathbf{k}(\mathbf{k})\rangle$, where $|u(\mathbf{k})\rangle$ is periodic part of Bloch wave. The Berry curvature maps of the valence band and the conduction band are shown in Figure 1e,d, respectively. The CBM and VBM have valley-contrasting Berry curvature associated with the Bloch electrons. Carriers with nonzero Berry curvature experience the effect of the external force analogous to the Lorentz force for a moving charge through magnetic flux regions. Under an in-plane electric field, the transverse velocity induced by Berry's curvature leads to a spatial separation of the carriers from two valleys. The spatially separated carriers are accumulated at different sides of the samples, resulting in a valley Hall effect. Based on our ab initio calculations, the honeycomb BP, BAs, BSb, GeC, SnC, SiC, $AgScP_2S_6$, $AgScP_2S_6$, and $CuSnP_2Se_6$ monolayers show similar valleytronic properties to h-BN monolayers, and their band structures and $\mathbf{k}$-resolved degree of optical polarization are shown in Figure S1.

Valley Quasi-Quantization. A periodic perturbation, such as the periodic electric field, Moire pattern, or periodic atomic doping, is referred to a quantum confinement, which can split the bands into a series of discrete electronic subbands. Here, subbands are tailored by suitable doping with low-concen-

DOI: 10.1021/acs.nanolett.7b00271
Nano Lett. 2017, 17, 2079−2087

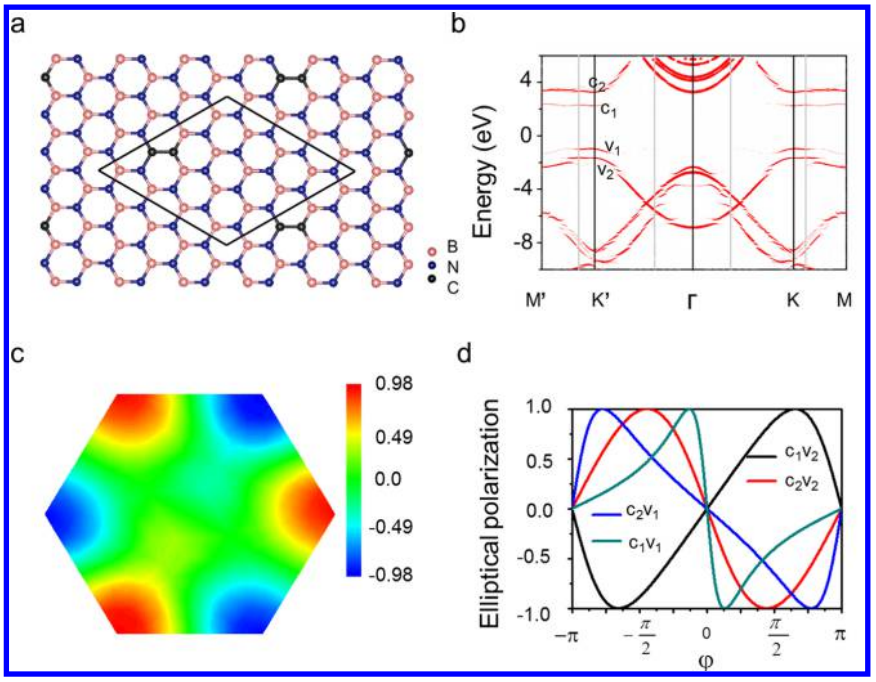

Figure 2. Valley quantization of carbon-doped h-BN monolayer. (a) 4 × 4 h-BN superlattice doped with two carbon atoms. The black, pink, and blue balls represent the C, B, and N atoms, respectively. (b) Unfolded band structure along the high symmetric lines. The bandgap between the first valence band (v_1) and the first conduction band (c_1) is 3.20 eV. The bandgap between the first valence band v_1 and the second valence band v_2 (or between the first conduction band c_1 and the second conduction c_2) is 0.72 (1.05) eV. (c) Degree of circular polarization in the folded BZ for the v_1 and c_1 subbands. (d) Degrees of elliptical polarization as a function of φ (phase angle of an elliptical photon).

tration carbon atoms. A selected crystalline structure and the corresponding dispersion relationship are shown in Figure 2a,b, and the resonant phonon−electron interaction splits pristine valleys into electronic subbands. The shown bands have been unfolded into the primitive-cell BZ of intrinsic h-BN monolayer.[26,27] Each patch can be viewed as a valley quasiparticle and contains discrete values of energy, valley magnetic moments, and charge carriers. According to Figure 2c, there is a Berry phase flux spreading across each subband in a valley. Thus, a momentum-space circumnavigation enclosing such a subband accumulates a constant of Berry phase.[12] By integrating the Berry curvature, the valley Chern number is obtained as

$$C_v = \frac{1}{2\pi}\int_{\mathrm{BZ}} \tau\Omega_n \, \mathrm{d}k^2 \tag{2}$$

where τ is the valley index. Carriers accumulate a Berry phase of $\pi \cdot C_v$ for either of the valleys due to 2π rotation of the pseudospin locked to the momentum. The integrating region corresponds to the full BZ of the folded bands of a superlattice. In the selected configuration, the Berry curvature is a smooth function owing to the bandgap opening and localized in the two valleys. Our calculations reveal that C_v = 0.104 by integrating the Berry curvature of the highest subband split from the valence band. Graphene doped with h-BN nanodots (high-concentration carbon-doped h-BN monolayer) can have an integer valley Chern number with C_v = 2 (details shown in Figure S2). A quantum valley Hall conductance $\frac{e^2}{h}C_v$ is obtained if the valley Chern number is nonzero. The valley Chern number is observable to the experiment through subtle signatures of the valley Hall effect. The quantum steps can be observed in valley Hall effect with an increasing carrier density, but there is no corresponding edge state. The valley Chern number is not necessary to be limited to a certain constant, but it can be discrete.

In addition, the energy of the photon absorbed by the valley and the wavelength of optical pumping are discontinuous due to a large bandgap (approximately 1 eV) between the subbands near the Fermi level of the doped h-BN monolayer. The bandgap between two the subbands is induced by the resonant electron−phonon interaction and heavily dependent upon carbon doping. The separated band structure is critical to protecting the valley from the interference of other parts of the BZ. On the other hand, the integration of the valley magnetic moment over the valley is a discontinuous value with the increasing carrier density.

Owing to the absence of the C_3 symmetry in h-BN monolayer, the valley-selective elliptical dichroism in periodically doped h-BN monolayer replaces the originally circular dichroism of intrinsic h-BN monolayer. A left-handed (right-handed) elliptically polarized photon can be selectively absorbed around the K' (K) point, while a right-handed (left-handed) one is completely prohibited. As known, a certain polarized state of a monochromatic light wave with electric field in the x−y planes yields E_x and E_y in the form of cosine. $E_x = A_x \cos(\omega t)$ and $E_y = A_y \cos(\omega t + \varphi)$, where θ is the phase retardation between E_x and E_y and $\gamma = \frac{E_x}{E_y}$ is the amplitude ratio. The coupling strength with optical fields of elliptical polarization is given by[28]

$$P_{\pm} = P_x + \gamma e^{\pm i\varphi} P_y \tag{3}$$

The k-resolved elliptical polarization is given by eq 1, where the first and second conduction bands and the first and second valence bands are assigned with indexes as c_1, c_2, v_1, and v_2, respectively. According to Figure 2d, the optical transition processes from the conduction bands to the valence bands

DOI: 10.1021/acs.nanolett.7b00271
Nano Lett. 2017, 17, 2079−2087

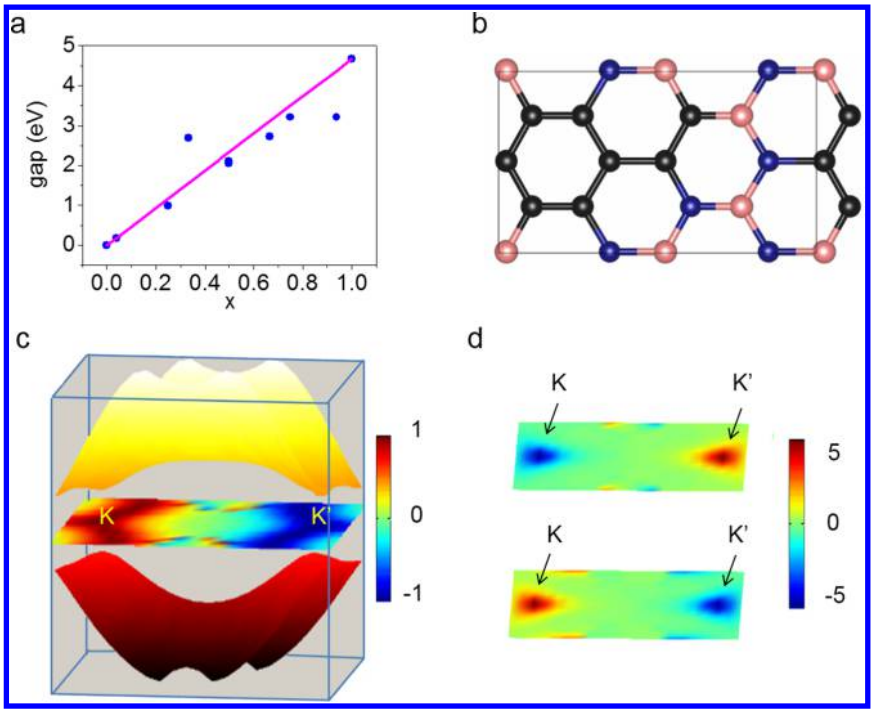

Figure 3. (a) Bandgap of $(BN)_x(C_2)_{1-x}$ as a function of doping concentration x. Blue dots come from the ab initio calculation, and the red line comes from to the atomic orbital theory (eq 5 in the main text). (b) A selected crystal structure of the hexagonal $(BN)_{0.5}(C_2)_{0.5}$ monolayer. (c) The bottom conduction band (yellow)) and the top valence band (red) of the selected $(BN)_{0.5}(C_2)_{0.5}$ monolayer. The bandgap is 1.78 eV. The rectangle in the middle is the Brillouin zone color-coded by the degree of circular polarization. The K and K' points are the crystal momentums of the band bottoms. (d) Berry curvature of the valence (upper) and conduction (lower) bands of the selected $(BN)_{0.5}(C_2)_{0.5}$ monolayer.

require different helicities. The peaks of the four curves are localized in distinct positions, and $\gamma(c_1v_1)$, $\gamma(c_1v_2)$, $\gamma(c_2v_1)$, $\gamma(c_2v_2)$ are 1.66, 0.767, 0.654, and 1.108, respectively. The selection rule at the K and K' points is elliptical with opposite helicity, so circular polarization cannot generate perfect valley polarization. By controlling the incident helicity, it is effective to engineer a population inversion of carriers between different subbands in order to achieve valley polarization between various band extrema. An elliptically polarized transition with orthogonal helicity allows for a perfect valley polarization between the first conduction and the first valence bands by properly controlling the values of γ, φ, and the pumping energy. In order to restrict valley polarized carriers in the second conduction or the second valence bands, we should increase the strength of the desired transition and decrease the unwanted transition by optimizing γ. If the valley polarization between the c_2 and v_2 subbands, for example, is needed, the values of γ and φ are set as 1.108 and 0.455π, respectively. The elliptical polarization for the various transition $\eta(c_2v_2)$, $\eta(c_1v_1)$, $\eta(c_1v_2)$, $\eta(c_2v_1)$ is -1.0, -0.418, -0.518, and 0.773, respectively. An elliptical polarization of 1 or -1 means that the elliptically polarized photon with certain helicity can only be absorbed by the K or K' valleys. The band indexes in vicinity of the valleys serve as another discrete degree of freedom apart from the valley degree of freedom, which shows great promise for harvesting and processing discrete information by energy and optical helicity locked to the crystal momentum.

Tunable Bandgap of the $(BN)_x(C_2)_{1-x}$ Monolayers. A valleytronic material with a tunable bandgap is expected owing to an urgent requirement for nanomaterials working as nanoscale circularly polarized light sources.[4,29] Technological advances in chemical vapor deposition (CVD) enable the successful synthesis of the large-scale layered structures $(BN)_x(C_2)_{1-x}$[23−25] by atomically hybridizing h-BN monolayer and graphene. The bandgap and the spin-split of hybrid structures can be controlled by the composition. Our finite calculations demonstrate that most of the possible configurations of $(BN)_x(C_2)_{1-x}$ have valley-contrasting Berry curvature, a pair of valley pseudospin, and valley-selective circular dichroism (see Figure 3 and Figure S3). There is a Berry's flux spreading across the tip of the massive Dirac cone of the $(BN)_x(C_2)_{1-x}$ monolayers. A circle enclosing either valley accumulates Berry phase in momentum space.

According to the atomic orbital theory, the homogeneous $(BN)_x(C_2)_{1-x}$ monolayers can be approximately described as follows:

$$|(BN)_x(C_2)_{1-x}\rangle = \sqrt{1-x}|\text{graphene}\rangle + \sqrt{x}|BN\rangle \quad (4)$$

Based on eq 4 the bandgap of the $(BN)_x(C_2)_{1-x}$ monolayers is given by

$$\Delta = 4.66x \quad (5)$$

eq 5 coincides very well with the calculated values, as shown in Figure 3a. In case of a small x, the $(BN)_x(C_2)_{1-x}$ monolayer is similar to pure h-BN monolayer and has a bandgap in the ultraviolet or deep ultraviolet region. With the increasing x, the bandgap can be modulated in the visible range. In another extremum of large x, the $(BN)_x(C_2)_{1-x}$ monolayer approaches to the noncentrosymmetric graphene and thus has a bandgap in the infrared or far-infrared region. Both noncentrosymmetric graphene and h-BN monolayer are good valleytronic materials, and thus the $(BN)_x(C_2)_{1-x}$ monolayers could inherit nontrivial valley pseudospin texture and phase flux from their parent systems.

Previous reports about valleytronics are well-described by the two-band $k\cdot p$ Hamiltonian[11,14] $H = at(\tau k_x\sigma_x + k_y\sigma_y) + \frac{\Delta}{2}\sigma_z$,

DOI: 10.1021/acs.nanolett.7b00271
Nano Lett. 2017, 17, 2079−2087

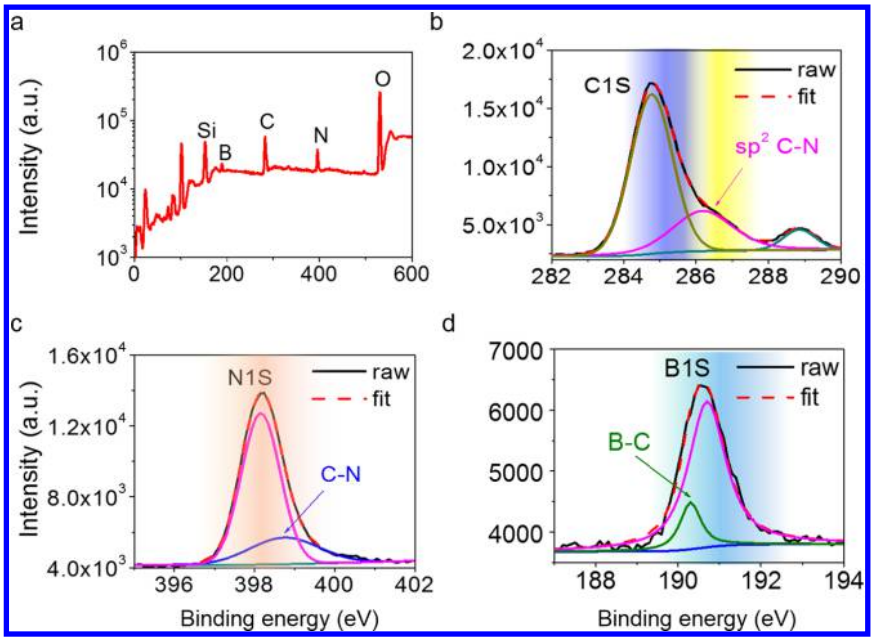

Figure 4. (a) XPS spectrum of $B_{0.92}NC_{2.44}$ sample with low-resolution detection. (b–d) XPS spectra of C1S, N1S, and B1S with high resolution.

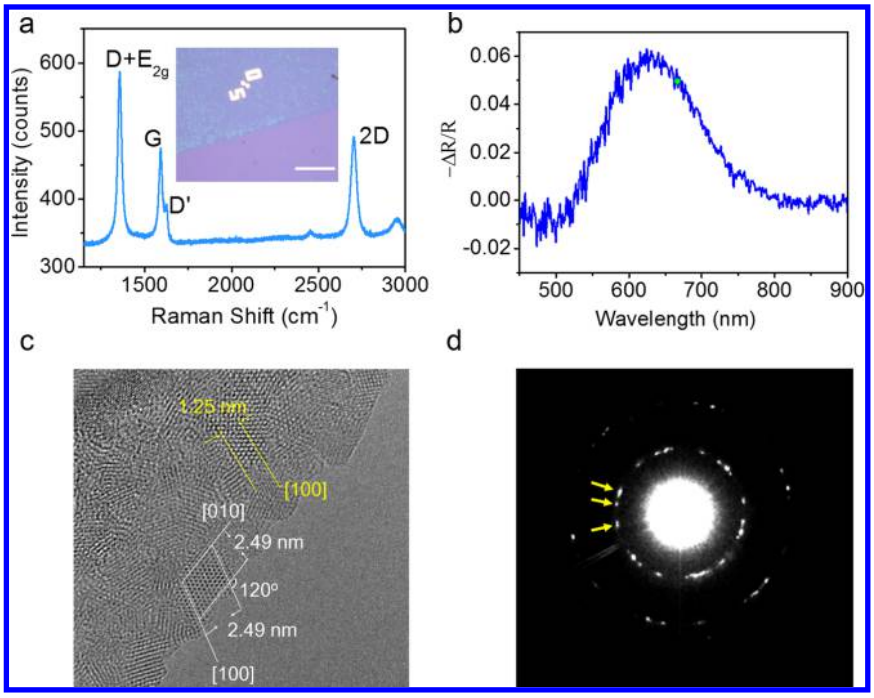

Figure 5. (a) Raman shifts and optical images of the samples on which micro-PL is performed, where $B_{0.92}NC_{2.44}$ is labeled (scale bar: 50 μm). (b) Differential absorption spectrum measured at 300 K. (c) High-resolution transmission electron microscopy images of the thin region. There are ten periods between the two parallel white lines in the directions of [1000] or [0100] and five periods between the two parallel yellow lines in the directions of [1000] or [0100]. Both measures indicate an interplane spacing distance of 0.249 nm. (d) A selected-area electron diffraction pattern for a few-layer region.

which is on the basis of the C_3 symmetry. However, the C_3 symmetry is broken in the most configurations of the $(BN)_x(C_2)_{1-x}$ monolayers. Some configurations of the $(BN)_x(C_2)_{1-x}$ monolayers are even tetragonal. Although the protection of the C_3 symmetry is absent, both the conduction and valence bands still display significant Berry curvature with opposite signs at the band edges (Figure 3 and Figure S3). As far as we know, the tetragonal 2D materials holding valley pseudospin have rarely been reported.[30,31] Some typical examples are selected to display in this article (tetragonal $(BN)_{0.5}(C_2)_{0.5}$ monolayer in Figure 3, hexagonal $(BN)_{0.75}(C_2)_{0.25}$ monolayer, and tetragonal $(BN)_{0.25}(C_2)_{0.75}$ monolayer in Figure S3), and they all exhibit a pair of valleys with direct bandgaps, valley-contrasting Berry curvature, and valley-selective circular polarization. More samples with different doping contents of carbon atoms are discussed in Figure S4 in the Supporting Information. An empirical rule can be summarized from the DFT calculations. A monolayer

DOI: 10.1021/acs.nanolett.7b00271
Nano Lett. 2017, 17, 2079–2087

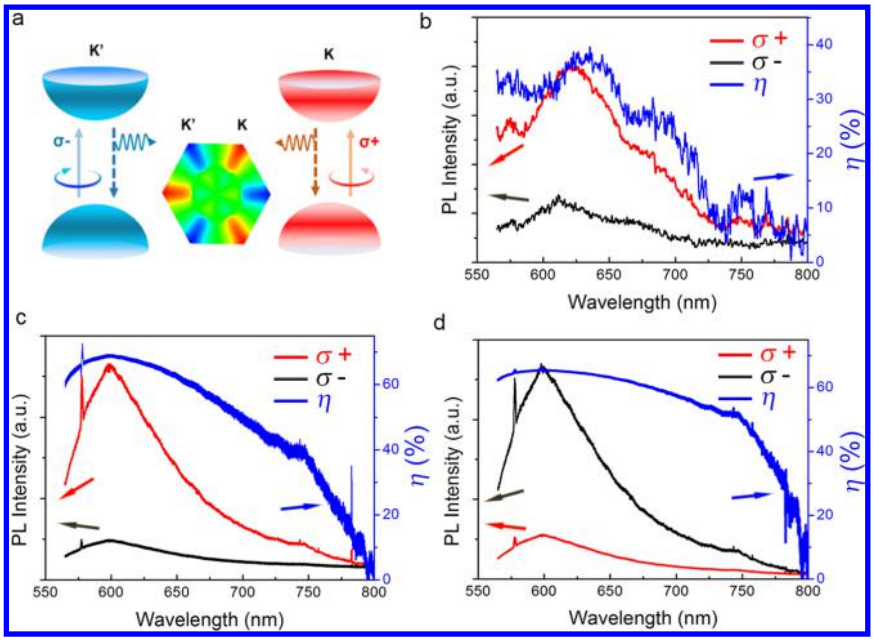

Figure 6. (a) Illustration of valley-contrasting circularly polarized PL process. Circularly polarized micro-PL of the $B_{0.92}NC_{2.44}$ sample at 300 K under σ^+ pump (b), at 77 K under σ^+ pump (c), and at 77 K under σ^- pump (d). The black and red curves correspond to the intensities of σ^- and σ^+ emission, respectively, and the blue one corresponds to the degree of circular polarization. The pumping laser has a wavelength of 488 nm.

$(BN)_x(C_2)_{1-x}$ structure has a pair of valley pseudospins if it has a honeycomb structure, the time reversal symmetry (namely, the absence of external magnetic field or magnetic impurity), the spatial inversion asymmetry, and a direct bandgap that is not located at time-reversal invariant momentum (such as such as the Γ and M points in the BZ). Such a pair of valley pseudospins will lead to a valley-contrasting circular dichroism, which is time-reversal symmetric. The valley-contrasting circular dichroism should increase with the decreasing temperature since the intervalley scattering is restricted at a low temperature. A detail mathematical derivation for this empirical rule is provided in the part of "mathematical derivation of the empirical rule" in the Supporting Information.

Experiment. The synthesis of carbon-doped BN samples was carried out by CVD using methane as carbon source and vaporized ammonia borane as boron and nitrogen sources. As shown in Figure 4a, the spectrum of X-ray photoelectron spectroscopy (XPS) exhibits characteristic peaks, including B1S, N1S, and O1S, as well as C1S. The XPS measurement was performed on a SiO_2/Si substrate, and thus the observed oxygen peak originates from the SiO_2 layer. The XPS spectrum of C atoms is composed of three characteristic peaks including C1S (284.72 eV), defect peak (288.83 eV), and sp^2 C−N (286.15 eV); the last peak proves the covalent bonding of C and N atoms as shown in Figure 4b.[32,33] The XPS spectrum of N atoms is composed of two peaks, the N1S peak (398.18 eV) and the C−N peak; the latter also suggests that part of N atoms bond with C atoms as shown in Figure 4c.[22] The peaks at a binding energy of 190.7 eV is attributed to B1S in h-BN, and the peak of 190.2 eV is ascribed to C−B bonding due to a lower electronegativity of C than N.[23,34] The C−N and C−B bonds are located at the boundaries between the h-BN and graphene domains, or the inner of the C doped h-BN domains or BN doped graphene domains, or the inner of the true ternary B−N−C domains.[23] The proportion of B:N:C atoms analyzed by the XPS is determined to be 0.21:0.23:0.56, and the sample is named as $B_{0.92}NC_{2.44}$ by the stoichiometry.

To further characterize the samples, the Raman shifts are measured under the excitation of 5 mW power (Figure 5a). A peak composed of E_{2g} photon mode of h-BN and D mode of graphene appears at 1356.7 cm^{-1}. Besides, G mode (1591.3 cm^{-1}), D′ mode (1625.6 cm^{-1}), and 2D mode (2703.5 cm^{-1}) of graphene are also observed. The D′ mode may result from the doping and atomic disorder. Different from the film of graphene/h-BN synthesized in previous report,[22] the Raman shifts of E_{2g} and D modes in our samples are at a higher frequency due to the defects in graphene and the h-BN sheets. The Raman shifts remain the same even after three months under the ambient condition (see Figure S5) at room temperature, indicative of a high stability of our sample. The inset of Figure 5a shows the optical image of $B_{0.92}NC_{2.44}$ on a 300 nm SiO_2/Si substrate. The $B_{0.92}NC_{2.44}$ film can be obviously distinguished by the color contrast. According to the XPS and Raman spectra, the h-BN and graphene domains predominate in the sample. This is consistent with the previous report that the h-BN and graphene are thermodynamically immiscible, preferring separation into different domains.[23] The D′ mode in the Raman spectrum indicates that the h-BN and graphene domains may be atomically doped.

The reflectance spectrum of the atomically thick $B_{0.92}NC_{2.44}$ is shown in Figure 5b. The reflectance spectrum gives a very broad peak across almost all of the visible range. This is attributed to the multidomain and polycrystalline features of the sample (with defects and atomic disorder). The strongest absorption peak centers at ∼625 nm showing a full-width at half-maximum of ∼200 nm. During the measurement of circularly polarized PL spectra, an excitation radiation wavelength of 532 nm, which holds a photon energy approaching to the absorption energy, is utilized to optimize the PL emission. The PL intensity of $B_{0.92}NC_{2.44}$ increases as laser power varies from 5 to 20 mW as shown in Figure S7a. The PL spectra show a wide range of fluorescence peaking at ∼625 nm (1.98 eV), which is consistent with the ab initio calculated bandgap (∼1.8

DOI: 10.1021/acs.nanolett.7b00271
Nano Lett. 2017, 17, 2079−2087

eV) of a possible configuration of the h-BNC_2 monolayer in Figure 3a.

The high resolution transmission electron microscopy (HRTEM) and selected-area electron diffraction images are shown in Figure 5c,d and Figure S6. The HRTEM shows that the $B_{0.94}NC_{2.42}$ sample contains multiple domains with a honeycomb structure. The interplane spacing distance of crystal planes (1000) or (0100) measured from the HRTEM image is 0.249 nm, which is consistent with those of h-BN (0.250 nm), graphene (0.248 nm), and honeycomb B−C−N ternary phases (~0.249 nm). The selected-area electron diffraction image shows three groups of hexagonal spots with a small rotation, which further confirms that our crystalline is in the regime of a honeycomb structure. Different groups of hexagonal diffraction spots indicate a rotation of the different domains by certain angles.

Based on the calculations in the theoretical part, the inequivalent valleys absorb and radiate photons with opposite circular polarized light. σ^+ (σ^-) circularly polarized excitation generates σ^+ (σ^-) luminescence as shown in Figure 6a. Detecting the difference in inverse helicity of luminescence excited by a certain circularly polarized light can characterize the valley polarization effect. According to eq 1, the degree of circular polarization of the radiative luminescence is described as $\eta = \frac{I(\sigma^+) - I(\sigma^-)}{I(\sigma^+) + I(\sigma^-)}$, where $I(\sigma^+)/I(\sigma^-)$ represents the radiative intensity of the right/left handed (σ^+/σ^-) PL emission. The right/left handed (σ^+/σ^-) PL emission are detected and compared in the visible spectral range indicating the valley-selective circular dichroism in this $B_{0.92}NC_{2.44}$ sample. A maximum η of ~40% is observed at a wavelength of 625 nm with σ^+ excitation radiation (10 mW) in an ultrahigh vacuum chamber (10^{-8} Pa) at room temperature, as shown in Figure 6b. This $B_{0.92}NC_{2.44}$ sample obeys the rule of valley-selective circular dichroism at visible spectral range. The less-than-perfect valley-contrasting circular polarization observed in the experiments is ascribed to the inevitable intervalley scattering and atomic disorder. In a controlled experiment, a luminescence excited by laser with the opposite helicity (σ^- excitation radiation) gives a similar but opposite degree of circular polarization with a maximum value about −40% (see Figure S7). As the temperature decreases, the intervalley scattering attenuates. A maximum circular polarization of ±70% is obtained at a wavelength of 615 nm for both the right- and left-handed optical pumping at a temperature of 77 K (see Figure 6c,d). To examine the energy (wavelength) dependence of the circular polarization, a pump laser with a wavelength of 488 nm is applied to conduct the experiments. The valley polarization effect fades because the excitation energy is far from the direct bandgap (Figure S7).

Discussions. Here we discuss the connection of our theoretical and experimental results. The HRTEM and selected-area electron diffraction experiments indicate that the sample indeed has a honeycomb structure. Apparently, the first condition for a monolayer $(BN)_x(C_2)_{1-x}$ structure to have a pair of valley pseudospins is met. The sample has time-reversal symmetry due to absence of magnetic impurity or external magnetic field, and the second condition to generate a pair of valley pseudospins is naturally satisfied. According to the Raman spectra, XPS, and the HRTEM, the $B_{0.94}NC_{2.42}$ sample is not a single phase and primarily consists of h-BN and graphene domains. Generally, h-BN domains here are always doped by C atom, and graphene domains are doped by B and N atoms.[23] Both the C doped h-BN domains and B, N doped graphene domains are typically inversion asymmetric. However, even if the sample contains pure h-BN domains and graphene domains, the formation of a superlattice of pure h-BN domains and graphene domains can still lead to inversion asymmetry. In addition to the three cases, the sample probably contains a small amount of true B−N−C ternary domains, which usually lack inversion symmetry. The four cases all can meet the third condition to generate a pair of valley pseudospins. Besides, the part with inversion symmetry has no influence on the observation of the valley polarization and can be easily deducted.

As is well-known, the indirect-gap PL is weak, and the direct-gap PL predominates in the PL spectra. As the temperature decreases, the PL is enhanced and keeps its main shape, also indicative of an effective direct bandgap. For a spinless system, circularly polarized light emission is not allowed at time-reversal invariant momentums according to time reversal symmetry. Our sample can emit circularly polarized photons. Thus, the sample has an effective direct bandgap not located at time-reversal invariant momentums. Obviously, the effective components of the sample meet the fourth condition to generate a pair of pseudospins (namely, a direct bandgap not located at the time-reversal invariant momentums).

Taken together, our sample meets all four criteria to generate a pair of pseudospins in a monolayer $(BN)_x(C_2)_{1-x}$ structure. The valley pseudospins should lead to a valley-contrasting circular dichroism, which is time-reversal symmetric. In fact, a robust circular polarization is observed for our sample at different temperatures and energies. The circularly polarized PLs under optical pumping with opposite helicity are exactly opposite, which indicates the circular polarization is time-reversal symmetric. The degree of circular polarization increases quickly with the decreasing temperature since the phonon-induced intervalley scattering is restricted at the lower temperature. The observed time-reversal symmetric and temperature-enhanced characters of the circular polarization are very consistent with the predicted valley-contrasting circular dichroism. Besides, the observed very wide range of circular polarization in PL spectra for our sample reflects that a variety of domains contribute to the circularly polarized PL. This is consistent with our assumption that there are a variety of B−N−C superlattices meeting the criterions to generate a pair of valley pseudospins. Therefore, our theory is well-supported by the experimental observation. In turn, the experimental phenomena are well-explained by the theory too.

Conclusions. In this work, we demonstrate a series of the $(BN)_x(C_2)_{1-x}$ monolayers holding excellent valleytronic properties and expand the applications of valleytronics to a wider spectral range from deep ultraviolet to far-infrared spectra. Our calculations reveal that 2-fold valley pseudospin can be realized beyond the limitation of the C_3 symmetry in the 2D systems. In the periodically doped h-BN monolayer, quantum steps of valley Hall conductance are expected by tuning the Fermi level across the isolated valleys owing to the resonant phonon−electron interaction. The prepared $B_{0.92}NC_{2.44}$ sample shows a maximum valley polarization effect with a helical degree of 40% at room temperature and up to 70% at 77 K. The tetragonal structure with valley-contrasting physics gives a clue of valleytronic physics beyond C_3 symmetry,[30,31] such as anisotropy of valleys in tetragonal structures (α-(BEDT-TTF)$_2I_3$[35]), spin-polarized valleytronics in ferromagnetic materials (CrF_3 monolayers[36]), and nonlinear

DOI: 10.1021/acs.nanolett.7b00271
Nano Lett. 2017, 17, 2079−2087

valleytronics in centrosymmetric systems (like $MgPSe_3$ and $MgPS_3$ monolayers[37]). The introduced concept of valley quantization in carbon-doped h-BN provides a wide field of valleytronics in the artificial superlattices, which promotes the development of valley physics and valleytronic devices.

Methods. *Calculation Details.* For all materials, we first carried out a geometry optimization using the VASP package within the framework of the projector augmented wave (PAW) pseudopotential method using a plane-wave basis set. A cutoff energy of 600 eV was applied. The Brillouin-zone integrations were carried on a denser than 9 × 9 × 1 **k**-mesh. In order to avoid interaction between the 2D materials and its periodic images, vacuum regions with thickness larger than 15 Å were applied. Both the atomic positions and the lattice constant were relaxed until the maximal force on each relaxed atom was smaller than 0.001 eV/Å. Spin−orbit coupling was not included in our calculations due to negligible relativistic effect of B, N, and C elements.

Sample Preparation and Characterization. The synthesis of carbon-doped BN flacks was carried out by chemical vapor deposition (CVD). By controlling the methane flow rate and the reaction pressure at different temperatures, the samples can be synthesized. Copper foil substrates were loaded into a quartz tube in a furnace and heated to 1005 °C with flowing 20 sccm H_2 and annealed at this temperature for 40 min. Then ammonia borane was heated to 350 K by a heating belt and introduced to the growth chamber together with 7 sccm methane. The growth lasted for 10 min with H_2 flow shut down. Finally, the system was cooled naturally to room temperature under 500 sccm Ar and 10 sccm H_2.

X-ray photoelectron spectra were carried on an AXIS-Ultra instrument from Kratos Analytical using monochromatic A_l K_α radiation (225 W, 15 mA, 15 kV) and low-energy electron flow for charge compensation. To compensate for surface charge effects, binding energies were calibrated using C1S hydrocarbon peak at 284.72 eV. Casa XPS software package was used to refine the original data. Raman shift and photoluminescence (PL) spectra were obtained using a home-built ultrahigh vacuum spectrometer (HORIBA iHR550 Raman) with a 600 g mm^{-1} grating under 10^{-8} Pa. The excitation wavelengths were 488 nm for Raman shifts and 532 nm for PL spectra, respectively. Each spectrum was acquired in 8 s to minimize the noise-to-signal ratio. In the optical system, two sets of linear polarizer and quarter-wave plate were integrated in the optical system. One was settled after laser device, and the other was settled before the spectrometer. The laser powers were directly measured before the lens system, which was different from the actual value incident on the sample. The laser power was attenuated when light passed through the lens system, and the incident power on the sample was proper for spectral measurement. The light spot was about 1.5 μm. A polarimeter systems (Thorlabs, PAX5710IR1-T) was utilized to carefully check the polarization of the light. The HRTEM and selected-area electron diffraction images were carried out on a JEOL 2100F field emission HRTEM system, which is equipped with a post specimen aberration corrector (CEOS) at 120 kV.

■ ASSOCIATED CONTENT

Supporting Information

The Supporting Information is available free of charge on the ACS Publications website at DOI: 10.1021/acs.nanolett.7b00271.

Valleytronic calculations of some other monolayers; electric structure of BN-doped graphene superlattice; electronic structures of the hexagonal $(BN)_{0.75}(C_2)_{0.25}$ and $(BN)_{0.25}(C_2)_{0.75}$ monolayers; mathematical derivation of the empirical rule; proposed structures for $(BN)_x(C_2)_{1-x}$ monolayers at different doping levels and the corresponding band and valleytronic calculations; supplementary calculations of the hexagonal $(BN)_x(C_2)_{1-x}$ monolayers. Raman shifts figure; HRREM images; photoluminescence in different conditions (PDF)

■ AUTHOR INFORMATION

Corresponding Authors

*E-mail: zhyfang@pku.edu.cn.
*E-mail: jinglu@pku.edu.cn.
*E-mail: jbyang@pku.edu.cn.

ORCID

Zhigang Song: 0000-0002-8355-6498
Ziwei Li: 0000-0002-2987-7186
Zheyu Fang: 0000-0001-5780-0728

Author Contributions

Z.S. and Z.L. contributed equally to this work.

Notes

The authors declare no competing financial interest.

■ ACKNOWLEDGMENTS

This work was supported by the National Key Research and Development Program of China (2017YFJC020149, 2015CB932403, 2016YFB0700901, 2016YFB0700600), the National Natural Science Foundation of China (Nos. 11374023, 61422501, 51371009, 50971003, 51171001, 11274016, 11674005, 61521004, and 11674012), the MOST Project of China (Nos. 2010CB833104 and 2013CB932604), the Singapore National Research Foundation under NRF RF (No. NRF-RF 2013-08), and National Program for Support of Top-notch Young Professionals.

■ REFERENCES

(1) Mak, K. F.; McGill, K. L.; Park, J.; McEuen, P. L. *Science* **2014**, *344*, 1489−1492.
(2) Zeng, H.; Dai, J.; Yao, W.; Xiao, D.; Cui, X. *Nat. Nanotechnol.* **2012**, *7*, 490−493.
(3) Mak, K. F.; He, K.; Shan, J.; Heinz, T. F. *Nat. Nanotechnol.* **2012**, *7*, 494−498.
(4) Zhang, Y. J.; Oka, T.; Suzuki, R.; Ye, J. T.; Iwasa, Y. *Science* **2014**, *344*, 725−728.
(5) Isberg, J.; Gabrysch, M.; Hammersberg, J.; Majdi, S.; Kovi, K. K.; Twitchen, D. J. *Nat. Mater.* **2013**, *12*, 760−764.
(6) Rycerz, A.; Tworzydło, J.; Beenakker, C. *Nat. Phys.* **2007**, *3*, 172−175.
(7) Song, Z.; Liu, C.-C.; Yang, J.; Han, J.; Ye, M.; Fu, B.; Yang, Y.; Niu, Q.; Lu, J.; Yao, Y. *NPG Asia Mater.* **2014**, *6*, e147.
(8) Tsai, W.-F.; Huang, C.-Y.; Chang, T.-R.; Lin, H.; Jeng, H.-T.; Bansil, A. *Nat. Commun.* **2013**, *4*, 1500.
(9) Zhuang, H. L.; Johannes, M. D.; Blonsky, M. N.; Hennig, R. G. *Appl. Phys. Lett.* **2014**, *104*, 022116.
(10) Xu, X.; Yao, W.; Xiao, D.; Heinz, T. F. *Nat. Phys.* **2014**, *10*, 343−350.
(11) Xiao, D.; Yao, W.; Niu, Q. *Phys. Rev. Lett.* **2007**, *99*, 236809.
(12) Xiao, D.; Chang, M. C.; Niu, Q. *Rev. Mod. Phys.* **2010**, *82*, 1959.
(13) Wang, Y. *Phys. Rev. B* **2007**, *77*, 235406.
(14) Xiao, D.; Liu, G.-B.; Feng, W.; Xu, X.; Yao, W. *Phys. Rev. Lett.* **2012**, *108*, 196802.

DOI: 10.1021/acs.nanolett.7b00271
Nano Lett. 2017, 17, 2079−2087

(15) Balog, R.; Jørgensen, B.; Nilsson, L.; Andersen, M.; Rienks, E.; Bianchi, M.; Fanetti, M.; Lægsgaard, E.; Baraldi, A.; Lizzit, S. *Nat. Mater.* **2010**, *9*, 315−319.
(16) Ni, Z.; Liu, Q.; Tang, K.; Zheng, J.; Zhou, J.; Qin, R.; Gao, Z.; Yu, D.; Lu, J. *Nano Lett.* **2012**, *12*, 113−118.
(17) Quhe, R.; Zheng, J.; Luo, G.; Liu, Q.; Qin, R.; Zhou, J.; Yu, D.; Nagase, S.; Mei, W.-N.; Gao, Z. *NPG Asia Mater.* **2012**, *4*, e6.
(18) Yang, W.; Chen, G.; Shi, Z.; Liu, C.-C.; Zhang, L.; Xie, G.; Cheng, M.; Wang, D.; Yang, R.; Shi, D. *Nat. Mater.* **2013**, *12*, 792−797.
(19) Gorbachev, R. V.; Song, J. C. W.; Yu, G. L.; Kretinin, A. V.; Withers, F.; Cao, Y.; Mishchenko, A.; Grigorieva, I. V.; Novoselov, K. S.; Levitov, L. S.; et al. *Science* **2014**, *346*, 448−451.
(20) Lundeberg, M. B.; Folk, J. A. *Science* **2014**, *346*, 422−423.
(21) Okada, M.; Sawazaki, T.; Watanabe, K.; Taniguch, T.; Hibino, H.; Shinohara, H.; Kitaura, R. *ACS Nano* **2014**, *8*, 8273−8277.
(22) Kubota, Y.; Watanabe, K.; Tsuda, O.; Taniguchi, T. *Science* **2007**, *317*, 932−934.
(23) Ci, L.; Song, L.; Jin, C.; Jariwala, D.; Wu, D.; Li, Y.; Srivastava, A.; Wang, Z.; Storr, K.; Balicas, L. *Nat. Mater.* **2010**, *9*, 430−435.
(24) Chang, C.-K.; Kataria, S.; Kuo, C.-C.; Ganguly, A.; Wang, B.-Y.; Hwang, J.-Y.; Huang, K.-J.; Yang, W.-H.; Wang, S.-B.; Chuang, C.-H. *ACS Nano* **2013**, *7*, 1333−1341.
(25) Liu, Z.; Ma, L.; Shi, G.; Zhou, W.; Gong, Y.; Lei, S.; Yang, X.; Zhang, J.; Yu, J.; Hackenberg, K. P. *Nat. Nanotechnol.* **2013**, *8*, 119−124.
(26) Allen, P. B.; Berlijn, T.; Casavant, D. A.; Soler, J. M. *Phys. Rev. B: Condens. Matter Mater. Phys.* **2013**, *87*, 085322.
(27) Huang, H.; Zheng, F.; Zhang, P.; Wu, J.; Gu, B.-L.; Duan, W. *New J. Phys.* **2014**, *16*, 033034.
(28) Song, Z.; Quhe, R.; Liu, S.; Li, Y.; Feng, J.; Yang, Y.; Lu, J.; Yang, J. *Sci. Rep.* **2015**, *5*, 13906.
(29) Yao, W. *NPG Asia Mater.* **2014**, *6*, e124.
(30) Rodin, A.; Gomes, L. C.; Carvalho, A.; Neto, A. C. *Phys. Rev. B: Condens. Matter Mater. Phys.* **2016**, *93*, 045431.
(31) Hanakata, P. Z.; Carvalho, A.; Campbell, D. K.; Park, H. S. *Phys. Rev. B: Condens. Matter Mater. Phys.* **2016**, *94*, 035304.
(32) Cheng, I. F.; Xie, Y.; Gonzales, R. A.; Brejna, P. R.; Sundararajan, J. P.; Kengne, B. F.; Aston, D. E.; McIlroy, D. N.; Foutch, J. D.; Griffiths, P. R. *Carbon* **2011**, *49*, 2852−2861.
(33) Majumdar, A.; Das, S. C.; Shripathi, T.; Heinicke, J.; Hippler, R. *Surf. Sci.* **2013**, *609*, 53−61.
(34) Miyamoto, Y.; Rubio, A.; Cohen, M. L.; Louie, S. G. *Phys. Rev. B: Condens. Matter Mater. Phys.* **1994**, *50*, 4976.
(35) Kobayashi, A.; Suzumura, Y.; Piéchon, F.; Montambaux, G. *Phys. Rev. B: Condens. Matter Mater. Phys.* **2011**, *84*, 075450.
(36) Zhang, W.-B.; Qu, Q.; Zhu, P.; Lam, C.-H. *J. Mater. Chem. C* **2015**, *3*, 12457−12468.
(37) Liu, J.; Li, X.-B.; Wang, D.; Lau, W.-M.; Peng, P.; Liu, L.-M. *J. Chem. Phys.* **2014**, *140*, 054707.

DOI: 10.1021/acs.nanolett.7b00271
Nano Lett. 2017, 17, 2079−2087